Aquaculture 627 (2027) 744627

Contents lists available at ScienceDirect

Aquaculture

journal homepage: www.elsevier.com/locate/aquaculture

In vitro experiments and thermodynamic modeling of mineral precipitation in synthetic fish pre-urine with varying calcium, magnesium, and phosphate: A mechanistic model of nephrocalcinosis

Cameron M. Emadi [a,*], Jon Olav Vik [b], Marius Takvam [c], Tom Ole Nilsen [c], Colin J. Brauner [a], Chris M. Wood [a]

[a] Department of Zoology, University of British Columbia, Vancouver, BC, V6T 1Z4, Canada
[b] Faculty of Chemistry, Biotechnology and Food Science, Norwegian University of Life Sciences, Norway
[c] Department of Biological Sciences, University of Bergen, Bergen, Norway

ARTICLE INFO

Keywords:
Aquaculture
Acid-base regulation
Hypercapnia
Kidney stones
Supersaturation
Salinity

ABSTRACT

The increasing prevalence of nephrocalcinosis ("kidney stones") in salmonid aquaculture has prompted several explanations, including elevated and fluctuating CO_2, and increased salinity. However, the role of risk factors is difficult to resolve due to confounding rearing conditions and physiological complexity. Here we expand an *in vitro* model that mimics CO_2-driven acid-base disturbances associated with nephrocalcinosis to systematically vary the ionic composition of synthetic salmonid pre-urine. We evaluate the individual and interactive effects of calcium, magnesium, and phosphate on mineral precipitation at 12 and 18 °C. Turbidity increased following the acid-base disturbance and varied among ionic treatments. Elevated calcium produced the largest and most rapid increases in precipitation, while phosphate amplified calcium-driven responses. In contrast, magnesium had minimal effects on precipitation magnitude. Increased temperature enhanced precipitation. Changes in dissolved ion concentrations and Ca:PO_4 loss ratios indicated preferential removal of calcium and phosphate. X-ray diffraction analysis tentatively identified poorly crystalline apatite under elevated calcium and phosphate, while an amorphous phase was detected when magnesium was also elevated. *In silico* simulations showed that simulated dahllite ion activity product at 0 h explained approximately 95% of the variation in turbidity at 8 h. Together, these results identify Ca availability and its interaction with PO_4 as major determinants of precipitation following CO_2-driven alkalosis, while demonstrating that thermodynamic modeling can quantitatively predict precipitation responses across ionic conditions. This study provides a controlled experimental-mathematical framework for isolating key risk factors contributing to nephrocalcinosis and highlights the importance of managing CO_2 dynamics and ionic loading in intensive aquaculture.

1. Introduction

Nephrocalcinosis remains a persistent production-associated disease in intensive aquaculture and is widely recognized as one of the most important health challenges in land-based production systems (Moldal et al., 2025). It is characterized by intrarenal deposition of mineral precipitates composed primarily of calcium (Ca), magnesium (Mg), and phosphate (PO_4) (Smart et al., 1979; Sommerset et al., 2024). Although the condition has been recognized for five decades (Landolt, 1975), its mechanistic basis remains incompletely understood, in part because multiple environmental, nutritional, developmental, and physiological factors converge during hatchery production (Pfalzgraff et al., 2025; Sissener et al., 2026; Takvam et al., 2023). An additional concern is the apparent emergence of other mineralization disorders in the renal system, including urinary stones, or urocystolithiasis (Dalum et al., 2025).

Nephrocalcinosis has been reported in both flow-through systems and recirculating aquaculture systems (RAS), indicating that its causes are not confined to a single production method (Klykken et al., 2022). However, several aspects of RAS operation may increase the likelihood of conditions that favor nephrocalcinosis. In RAS, reduced water exchange allows progressive accumulation of dissolved ions derived from feed inputs, and chemical additions used for pH and alkalinity control.

* Corresponding author at: Department of Zoology, 6270 University Blvd, Vancouver, BC V6T 1Z4, Canada.
E-mail address: Cameron.Emadi@ubc.ca (C.M. Emadi).

https://doi.org/10.1016/j.aquaculture.2026.744627
Received 9 July 2026; Received in revised form 12 October 2026; Accepted 14 October 2026
Available online 16 October 2026
0044-8486/© 2026 The Authors. Published by Elsevier B.V. This is an open access article under the CC BY license (http://creativecommons.org/licenses/by/4.0/).

Buffering agents frequently contain Ca-based compounds or bicarbonate (HCO_3^-), while the use of seawater or sea salts during smoltification increases overall ionic strength and hardness (Sissener et al., 2026). Consistent with this, recent large-scale production analyses have identified elevated and fluctuating CO_2 concentrations, elevated water hardness (Ca, Mg), increasing rearing salinity and dietary Ca, Mg, and PO_4 as significant predictors of nephrocalcinosis severity (Klykken et al., 2023; Minarova et al., 2023; Sissener et al., 2026; Takvam et al., 2023). These findings suggest that both acid-base disturbance and ionic composition contribute to disease risk. However, while such analyses identify important associations, the extent to which these factors act independently, synergistically, or through shared environmental drivers within intensive production systems remains unclear.

Early work by Smart et al. (1979) proposed that elevated CO_2 exposure (hypercapnia) could promote mineral precipitation through HCO_3^- accumulation and increased urine pH during hypercapnia. While this explanation identified a potential link between CO_2 exposure and precipitation, it did not account for the dynamic conditions under which mineral formation may be initiated. More recently, this concept has been developed into a mechanistic and physiological framework (Takvam et al., 2023), in which sustained hypercapnia is associated with elevated plasma HCO_3^- (metabolic compensation of respiratory acidosis) in the blood, and a subsequent rapid decline in ambient partial pressure of carbon dioxide (PCO_2) produces a transient alkalosis in the blood and pre-urine, which promotes mineral precipitation in the latter. In a controlled *in vitro* model to test this hypothesis, we previously demonstrated that a rapid decline in PCO_2 following HCO_3^- compensation is sufficient to induce measurable mineral precipitation, and that elevated temperature further amplifies this response (Emadi et al., 2026). In that study, however, ionic composition in the synthetic pre-urine was held constant at concentrations representative of baseline salmonid plasma. This approach did not account for changes in ionic composition of the pre-urine that may occur during acid-base disturbances or increased ionic loading in intensive aquaculture systems, limiting evaluation of how variation in ionic composition influences mineral precipitation under these CO_2 driven conditions.

Mineral characterization of nephrocalcinosis deposits provides insight into the chemical conditions that may underlie these associations. Klykken et al. (2022) characterized deposits as being dominated by "amorphous carbonate apatite" ($Ca_{10}(PO_4)_6CO_3$), frequently accompanied by Mg containing PO_4 phases including struvite ($MgNH_4PO_4{\cdot}6H_2O$), whitlockite ($MgCa_8(PO_4)_6$), brushite ($CaHPO_4{\cdot}H_2O$), and newberyite ($MgHPO_4{\cdot}3H_2O$). Notably, all major phases contain PO_4, and most incorporate Ca and/or Mg, consistent with precipitation occurring under supersaturated conditions. From a chemical perspective, the degree of saturation is determined by the ion activity product (IAP) of precursor ions relative to the equilibrium solubility product (K_{sp}) of a given mineral phase, commonly expressed as the saturation index ($SI = \log_{10}(IAP/K_{sp})$). When IAP exceeds K_{sp} ($SI > 0$), precipitation is thermodynamically favorable (Ratkalkar and Kleinman, 2011; Song et al., 2002).

The composition of nephrocalcinosis deposits points to a need to determine how variation in ionic chemistry influences precipitation under an identical acid-base trajectory. Moreover, the varying compositions of different nephrocalcinosis deposits suggests that changes in individual ionic components could differentially influence nucleation kinetics, precipitation magnitude, or mineral phase formation (Ratkalkar and Kleinman, 2011). The present study therefore extends the previously validated acid-base framework by experimentally manipulating Ca, Mg, and PO_4 concentrations individually and in combination within synthetic pre-urine using a well-developed *in vitro* model (Emadi et al., 2026). These manipulations were designed to reflect conditions relevant to intensive aquaculture systems, where environmental ion concentrations increase through feed inputs, buffering agents, and salinity adjustments, leading to elevated ionic concentrations in body fluids. Experiments were conducted at 12 °C and 18 °C because they are relevant to intensive aquaculture conditions and were previously shown to produce elevated mineral precipitation in this *in vitro* system, allowing evaluation of the effects of temperature-ion interactions on precipitation dynamics (Emadi et al., 2026).

Turbidity, precipitate mass, and changes in dissolved ion concentrations were used to quantify mineral formation over time following a rapid decline in PCO_2 after HCO_3^- compensation, while X-ray powder diffraction (XRD) was used to characterize representative precipitates. This reduction in PCO_2, in the presence of elevated HCO_3^-, induces an alkalosis that is proposed to act as a trigger for mineral precipitation. Together, these approaches were used to evaluate how variation in ionic composition influences precipitation responses and the underlying thermodynamic driving force, quantified as IAP and SI. This approach allowed us to determine whether precipitation outcomes were consistent with thermodynamic supersaturation under the acid-base conditions hypothesized to initiate nephrocalcinosis.

2. Materials and methods

2.1. Solution preparation

The experimental setup was adapted from a previously described *in vitro* acid-base model (Emadi et al., 2026), with modifications to solution composition and experimental conditions. This approach tested the hypothesis that rapid declines in PCO_2 following HCO_3^- compensation promote mineral precipitation. Synthetic fish pre-urine was prepared using a modified Cortland saline (Wolf, 1963), which was adjusted to approximate salmonid plasma ion composition by setting HCO_3^- concentration to 8 mmol L^{-1} and reducing NaCl by an equimolar amount to maintain osmolality. This adjusted composition served as the control (1×) solution (see the Control column in both Table 1 and Table 2). Ionic treatments were generated by doubling the amounts of $CaCl_2{\cdot}2H_2O$, $MgSO_4{\cdot}7H_2O$, or $NaH_2PO_4{\cdot}H_2O$ required in the control formulation, resulting in twofold increases in Ca, Mg, and PO_4, respectively. These ions were elevated individually, in pairs, and in combination to produce a full factorial design. The resulting salt molarities and corresponding ionic composition (mmol L^{-1}) are presented in Tables 1 and 2 respectively.

For clarity throughout the manuscript, treatments are referred to using a shorthand notation indicating which ions were elevated relative to control. Ca, Mg, and PO_4 treatments are denoted as 2 × [Ca], 2 × [Mg], and 2 × [PO_4] respectively where each represents a twofold increase relative to the control formulation. Combination treatments are indicated by listing the relevant ions (*e.g.*, 2 × [Ca + Mg + PO_4]).

For each trial, a fresh 2-L batch of Cortland saline solution was prepared and divided into four acid-washed 500-mL Erlenmeyer flasks to avoid contamination from residual precipitate. During experiments, each flask was continuously aerated with the appropriate CO_2 gas mixture for the respective experimental phase and stirred with a magnetic stirrer (IKA RO 5 power S1, IKA-Werke GmbH & Co. KG, Staufen, Germany) to maintain homogeneity and stabilize the target PCO_2.

2.2. Temperature control

All experiments were conducted at either 12 °C or 18 °C. A large acrylic tank (dimensions: 46 cm × 27 cm × 20.5 cm) was used as a water bath and placed on top of the stirrer. Temperature was controlled using a water chiller unit with a submerged coil (Model 1160S, VWR International, Radnor, PA, USA), and circulation was maintained with a small submersible pump to ensure uniform conditions throughout the bath. Temperature was monitored with the built-in thermometer of the ROSS Ultra Triode pH electrode (Orion, Thermo Fisher Scientific Inc., Waltham, MA, USA) and a mercury thermometer placed in the reservoir. Solution temperature remained stable throughout the experiments, with within-flask standard deviations ≤0.30 °C.

Table 1
Nominal salt concentrations (mmol L^{-1}) used to prepare each treatment solution. All treatments were derived from a control formulation mimicking freshwater salmonid plasma, with a fixed HCO_3^- concentration (8 mmol L^{-1}). Experimental conditions involved a fully factorial design in which the concentrations of calcium ($CaCl_2{\cdot}2H_2O$), magnesium ($MgSO_4{\cdot}7H_2O$), and phosphate ($NaH_2PO_4{\cdot}H_2O$) were individually or jointly doubled relative to the control. Treatments are labeled accordingly. Values reflect the molar concentration of each salt compound in solution.

Salt	Control	2 × [Ca]	2 × [Mg]	2 × [PO_4]	2 × [Ca + Mg]	2 × [Ca + PO_4]	2 × [Mg + PO_4]	2 × [Ca + Mg + PO_4]
NaCl	127.96	127.96	127.96	127.96	127.96	127.96	127.96	127.96
KCl	5.10	5.10	5.10	5.10	5.10	5.10	5.10	5.10
$CaCl_2{\cdot}2H_2O$	1.56	3.13	1.56	1.56	3.13	3.13	1.56	3.13
$MgSO_4{\cdot}7H_2O$	0.93	0.93	1.87	0.93	1.87	0.93	1.87	1.87
$NaHCO_3$	8.00	8.00	8.00	8.00	8.00	8.00	8.00	8.00
$NaH_2PO_4{\cdot}H_2O$	2.97	2.97	2.97	5.94	2.97	5.94	5.94	5.94

Table 2
Nominal ionic composition (mmol L^{-1}) of each treatment solution. Ionic concentrations were calculated based on the dissociation of salts added to a modified Cortland saline formulation designed to mimic freshwater salmonid plasma, with a fixed HCO_3^- concentration (8 mmol L^{-1}). Treatments followed a fully factorial design in which the concentrations of calcium, magnesium, and phosphate were individually or jointly doubled relative to the control. Values reflect the total molar concentration of each ion contributed by all relevant salt sources.

Ion	Control	2 × [Ca]	2 × [Mg]	2 × [PO_4]	2 × [Ca + Mg]	2 × [Ca + PO_4]	2 × [Mg + PO_4]	2 × [Ca + Mg + PO_4]
Na^+	138.93	138.93	138.93	141.90	138.93	141.90	141.90	141.90
K^+	5.10	5.10	5.10	5.10	5.10	5.10	5.10	5.10
Ca^{2+}	1.56	3.13	1.56	1.56	3.13	3.13	1.56	3.13
Mg^{2+}	0.93	0.93	1.87	0.93	1.87	0.93	1.87	1.87
Cl^-	136.19	139.32	136.19	136.19	139.32	139.32	136.19	139.32
HCO^{3-}	8.00	8.00	8.00	8.00	8.00	8.00	8.00	8.00
SO_4^{2-}	0.93	0.93	1.87	0.93	1.87	0.93	1.87	1.87
$H_2PO_4^-$	2.97	2.97	2.97	5.94	2.97	5.94	5.94	5.94

2.3. PCO_2 and pH manipulation

The experimental design followed the general multi-phase framework described in Emadi et al. (2026), with modifications to incorporate ionic manipulations. The phases simulated a respiratory acidosis (PCO_2 elevation), physiological compensation through HCO_3^- elevation, and subsequent alkaline shift caused by a rapid reduction in PCO_2. Fig. 1 shows a representative experiment illustrating the pH across the experimental phases which are described below.

In phase 1 (initial equilibration), each flask was aerated with premixed air-CO_2 gas (0.5% CO_2, research grade, Linde Canada Inc., Mississauga, ON, Canada) to mimic control venous PCO_2 values (see Table 3 for conversion of commonly used CO_2 units). pH was monitored using a Ross Ultra pH/ATC Triode electrode (Orion 8302BNUMD) connected to a Star A211 pH meter (Thermo Fisher Scientific Inc., Waltham, MA, USA), calibrated daily with standard pH 4.0, 7.0, and 10.0 buffers (VWR Chemicals, Radnor, PA, USA).

Table 3
Estimated partial pressure and dissolved concentration of CO_2 for each gas mixture and temperature treatment. Values represent the calculated PCO_2 in torr and kilopascals (kPa), and the corresponding dissolved CO_2 concentrations in mg/L at equilibrium in freshwater.

Temperature (°C)	CO_2 (%)	PCO_2 (torr)	PCO_2 (kPa)	Dissolved CO_2 (mg L^{-1})
12	0.5	3.7	0.5	11.0
12	2	15.0	2.0	44.2
18	0.5	3.7	0.5	9.1
18	2	14.9	2.0	36.5

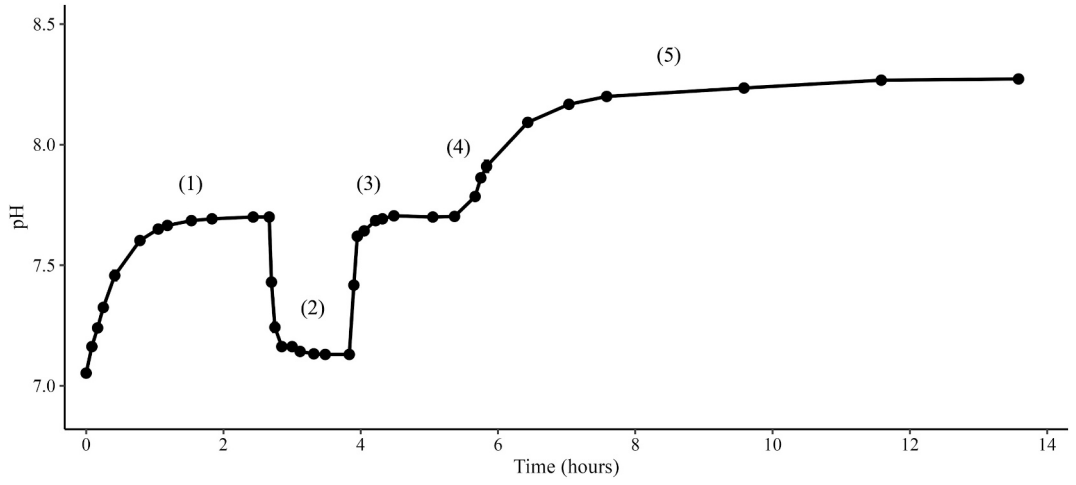


Fig. 1. Mean pH trace from a representative treatment across four replicate flasks. Phase (1) represents the initial equilibration (~2 h) to 0.5% CO_2. Phase (2) shows the decrease in pH during respiratory acidosis (2% CO_2). Phase (3) represents restoration of pH to baseline *via* $NaHCO_3$ addition (compensated state). Phase (4) marks the rapid increase in pH following reduction in PCO_2 (trigger). Phase (5) spans the post-trigger period during which precipitation dynamics were monitored. Values are mean ± SEM ($N = 4$), although error bars are smaller than the symbol for most time points.

Preliminary tests revealed that treatments with elevated PO_4 exhibited a lower pH during the initial equilibration. To account for this, 1–2 mL of $NaHCO_3$ (1 mol L^{-1} stock) was added to each flask prior to equilibration. Following solution preparation, flasks were gassed with the 0.5% CO_2 in air mixture for ~2 h until pH stabilized at an average of 7.61 ± 0.01, which was recorded as the baseline reference. Throughout the experiment, pH was continuously monitored and recorded for each flask.

In phase 2, PCO_2 was elevated to 2% CO_2 using a Wösthoff gas mixing pump (DIGAMIX Type 6KM 422; Wösthoff Messtechnik GmbH, Bochum, Germany), which blended pure CO_2 with ambient air to simulate respiratory acidosis conditions representative of high-density aquaculture systems. Under these conditions, pH decreased and stabilized at 7.04 ± 0.01. In phase 3, the flasks were titrated with 1 mol L^{-1} $NaHCO_3$ solution, added incrementally by micropipette while continuously monitoring pH, to restore pH to the baseline value (7.60 ± 0.01) and simulate a compensated respiratory acidosis state. In phase 4 (the "trigger"), PCO_2 was rapidly reduced by aerating with 0.5% CO_2, causing a rapid increase in pH as HCO_3^- remained elevated following compensation. This transition simulated an abrupt reduction in ambient PCO_2. In phase 5, PCO_2 was held at 0.5% CO_2 to track the progression of precipitation over time, using turbidity measurements as described below.

2.4. TCO_2, PCO_2, and HCO_3^- determinations

Total CO_2 (TCO_2; mmol L^{-1}) and turbidity were measured after equilibration at the end of each experimental phase, as well as at 2, 4, 6, and 8 h post-trigger (*i.e.*, following the rapid reduction of PCO_2). pH values measured as described in Section 2.3 were used in subsequent calculations. Total CO_2 was measured using a Model 965 Total CO_2 analyzer (Corning Instruments, Corning, NY, USA).

Experimental treatments altered the ionic composition of the test solutions. Accordingly, differences in molarity, sodium concentration, and ionic strength were incorporated into the calculation of pK' and the CO_2 solubility coefficient (αCO_2). These calculations also accounted for the addition of $NaHCO_3$ during phase 3 (compensation) and the initial pH adjustment required for elevated PO_4 treatments in phase 1.

Measured values for pH and TCO_2, together with estimates of pK' and αCO_2 based on Boutilier et al. (1984), were used to calculate PCO_2 by rearrangement of the Henderson-Hasselbalch equation (Boutilier et al., 1984; Brauner et al., 2000; Mota et al., 2020):

$$PCO_2 = \frac{TCO_2}{\alpha CO_2 \cdot \left(10^{(pH-pK')} + 1\right)}$$

HCO_3^- concentrations were then calculated as:

$$HCO_3^- = TCO_2 - (\alpha CO_2 \cdot PCO_2)$$

2.5. Turbidity, gravimetric, and X-ray diffraction analyses

Turbidity in each flask was measured using an Orion AQUAfast AQ3010 turbidity meter (Thermo Fisher Scientific, Waltham, MA, USA). A single turbidity vial was used for the entire experiment, with each sample measured twice and the values averaged. Samples were collected under continuous stirring to ensure uniform suspension of precipitate. For each measurement, 10-mL of solution was withdrawn with a manual pipette filler (Smoothie, VWR International, Radnor, PA, USA) and transferred into the turbidity vial. Solutions were gently inverted three times before measuring to suspend any precipitate while minimizing air bubble formation. Between samples, the vial was rinsed thoroughly with Milli-Q water and dried.

Following turbidity measurements during the initial equilibration and respiratory acidosis phases, 2 mL aliquots were removed from the 10 mL turbidity samples, transferred into microcentrifuge tubes, and acidified with 1% nitric acid (HNO_3) for subsequent ionic analysis. Dissolved ion levels were measured in samples from the compensated respiratory acidosis state (phase 3, designated as time 0) and subsequent time-course samples (2, 4, 6, 8 h), where the entire 10 mL turbidity sample was transferred into pre-dried 15 mL centrifuge tubes and centrifuged at ~1100 *g* for 5 min to separate precipitate from the supernatant (International Equipment Co., Boston, MA, USA). The supernatant was decanted and transferred into microcentrifuge tubes, acidified with 1% HNO_3, and stored at 4 °C. Any remaining supernatant was carefully removed to expose the pellet, which was dried without washing at 50 °C for 48 h. Precipitate mass was determined gravimetrically by subtracting the mass of the empty dried centrifuge tube from the final mass of the tube containing precipitate.

Following gravimetric analysis, dried precipitates from representative treatments were analyzed by powder X-ray diffraction (XRD) to characterize mineral phase composition and crystallinity. Samples from the 2 × [Ca], 2 × [Ca + PO_4], and 2 × [Ca + Mg + PO_4] treatments at the 8 h endpoint were selected for analysis, with two replicate samples analyzed per treatment. Samples were lightly ground in a corundum mortar and pestle and mounted on a low background quartz plate using ethanol. Continuous-scan X-ray powder-diffraction data were collected over a range of 4–80°2θ using Co-Kα radiation and a 10 mm fixed area, variable intensity divergence slit, on a Bruker D8 Endeavor Bragg-Brentano diffractometer equipped with LynxEye-XE-T detector (Bruker, Billerica, Massachusetts, USA). Diffractograms were analyzed using the International Centre for Diffraction Database PDF-5 and Search-Match software by Bruker.

2.6. Ionic analyses

Ca and Mg concentrations were measured using flame atomic absorption spectroscopy (FAAS; Varian, California, USA). Samples collected following centrifugation were diluted in ultrapure water with 1% $LaCl_3$ and 0.1% trace metal grade HNO_3 (Fisher Chemical, Canada). Analyses were performed using the manufacturer's recommended settings within the Spectra AA software. Soluble reactive PO_4 was quantified using the molybdenum blue colorimetric method (Murphy and Riley, 1962), following a protocol adapted from the *Limnological Methods Manual* (Program, 2011). PO_4 standards (0–20 μM phosphate) were prepared, and samples were diluted 300× (control, 1 × [PO_4]) or 600× (2 × [PO_4] treatments) to fall within the linear range of the assay. The mixed reagent was prepared fresh prior to analysis, and absorbance was measured at 850 nm using a microplate reader (SpectraMax 190, Molecular Devices). PO_4 concentrations were calculated from the standard curve and corrected for dilution.

2.7. Thermodynamic modeling of saturation state

To evaluate the thermodynamic driving force for precipitation across treatments, ion activity products (IAP) and saturation indices (SI) were calculated using PHREEQC version 3 (Parkhurst and Appelo, 2013), implemented through the *phreeqc* R package (Charlton et al., 2014). Simulations incorporated experimentally measured solution compositions from each experimental stage and modeled the experimental acid-base trajectory up to the immediate post-trigger condition following the reduction in PCO_2. IAP and SI were then calculated for the resulting post-trigger state.

Saturation index was expressed as:

$$SI = \log_{10}\left(\frac{IAP}{K_{sp}}\right)$$

where positive SI values indicate supersaturation. Ion activities were calculated using PHREEQC activity-coefficient models that account for ionic strength and electrostatic interactions in solution.

Multiple Ca, Mg, and PO_4 containing minerals relevant to nephrocalcinosis were evaluated based on mineral phases reported by

Klykken et al. (2022) and those available within PHREEQC databases. Among the databases distributed with PHREEQC, *llnl.dat* provided the equilibrium solubility products (K_{sp}) for most mineral phases and contained the greatest overall overlap with the mineral phases identified in deposits, although several mineral formulae differed slightly from those reported by Klykken et al. (2022). However, "amorphous carbonate apatite", the dominant mineral reported in nephrocalcinosis deposits by Klykken et al. (2022), was not directly available within standard PHREEQC databases. Therefore, dahllite ($Ca_{10}(PO_4)_6(CO_3)_{0.5}(OH)$) was used as a thermodynamic proxy for carbonate containing calcium phosphate phases. Thermodynamic parameters for dahllite, including K_{sp}, were obtained from the Joint Expert Speciation System (JESS) database (Bonet et al., 2023), converted to PHREEQC-compatible format, and incorporated into the model database. Additional details regarding PHREEQC implementation and database modifications are provided in Supplementary Methods (Thermodynamic Modeling).

2.8. Statistical analyses

All statistical analyses were conducted in R version 4.4.2. Statistical significance was assessed at $\alpha = 0.05$. Turbidity was measured at 0, 2, 4, 6, and 8 h for each treatment and temperature, with four replicate flasks per treatment and temperature.

For visualization of turbidity trajectories, values were first averaged across replicate flasks at each timepoint, and the standard error of the mean (SEM) was calculated. To illustrate the temporal precipitation dynamics, the averaged turbidity time series for each treatment and temperature were fitted with a Michaelis-Menten type function:

$$y = \frac{B_{max} \cdot t}{K_{0.5} + t}$$

where y is turbidity (NTU), t is time (h), B_{max} represents the asymptotic maximum turbidity, and $K_{0.5}$ is the time required to reach half of B_{max}. This function was used only as a nonlinear smoothing model to represent the rapid early increase in turbidity followed by a progressive slowing of the response. Nonlinear regression was performed using the *nlsLM* function from the *minpack.lm* package, with parameter estimates constrained to be non-negative (Elzhov et al., 2023). Parameter estimates (B_{max} and $K_{0.5}$) were obtained by fitting the model to the data using nonlinear regression. Fitted curves were overlaid on the averaged data points, with SEM error bars indicating variation among replicate flasks. Parameter estimates were used to generate the fitted curves and were not subjected to statistical testing.

To quantify precipitation rates following the experimental trigger, turbidity measurements from the compensated stage (0 h) and 2 h were analyzed. This interval was selected because it encompassed the period of most rapid turbidity increase. Turbidity data were analyzed using a linear mixed-effects model (lme4 package) with time (0 and 2 h), ion treatment, temperature (12 °C or 18 °C), and their interactions included as fixed effects, and flask included as a random effect to account for the repeated measures within each flask (Bates et al., 2015). Precipitation rates (NTU h^{-1}) were estimated as treatment-specific slopes of turbidity *versus* time using the *emtrends* function in the emmeans package (Lenth, 2025). Pairwise comparisons of slopes were conducted using Tukey-adjusted contrasts. Model assumptions were evaluated using residual diagnostic plots to assess residual normality and homogeneity of variance.

Final turbidity values at 8 h were analyzed using a two-way ANOVA model with ion treatment, temperature, and their interaction included as fixed effects. Data were log-transformed prior to analysis to meet assumptions of normality and homogeneity of variance, which were satisfied following transformation (Shapiro-Wilk, $p = 0.463$; Levene's test, $p = 0.141$). Following the ANOVA, pairwise comparisons of estimated marginal means were conducted using Tukey-adjusted contrasts.

Net changes in Ca, Mg and PO_4 were calculated as the difference between concentrations at 8 h and the compensated state for each flask. Ion concentration data were analyzed separately for each ion using two-way ANOVA with ion treatment, temperature and their interaction as fixed effects. For Ca and Mg, the treatment × temperature interaction was not significant. Therefore, treatment effects were compared using a reduced model containing the treatment and temperature, but no interaction term followed by Tukey-adjusted pairwise comparisons of estimated marginal means. For PO_4, where a significant treatment × temperature interaction was detected, *post hoc* comparisons among treatments were conducted within each temperature using Tukey-adjusted pairwise contrasts of estimated marginal means. Model assumptions were assessed using residual diagnostic plots to evaluate residual normality and homogeneity of variance.

To evaluate whether the dissolved ion losses between the compensated state (0 h) and 8 h were consistent with candidate mineral phases, molar ratios of Ca, Mg, and PO_4 were calculated from the ion losses for each flask. Ion losses were calculated as the decrease in concentration from the compensated state (0 h) to 8 h. Ratios were normalized to $PO_4 = 1$ to facilitate comparison with expected mineral stoichiometries, as PO_4 is a component of all mineral phases reported by Klykken et al. (2022). Ratios were averaged within each treatment and temperature group and expressed as mean ± SEM. These ratios were used as a mass-balance indicator of precipitate composition. Ratios are most meaningful in treatments exhibiting substantial ion loss, whereas values in treatments with minimal or variable ion change should be interpreted cautiously.

Lastly, the relationship between turbidity and precipitate mass was evaluated using linear regression, with turbidity included as a predictor and precipitate mass as the response variable. The model was fitted across all treatments and temperatures.

3. Results

3.1. Precipitation accumulation rates following the trigger (0–2 h)

Turbidity increased most rapidly during the first 2 h after the trigger in treatments containing elevated Ca in combination with PO_4 and/or Mg, whereas treatments without elevated Ca showed little change relative to controls (Fig. 2A). The 2 × [Ca] treatment alone showed a strong temperature-dependent response, differing from controls at 18 °C but not at 12 °C. Estimated precipitation rates in treatments with elevated Ca ranged from ~6 to ~81 NTU·h^{-1} at 12 °C and from ~45 to ~82 NTU·h^{-1} at 18 °C. In contrast, treatments without elevated Ca (2 × [Mg], 2 × [PO_4], 2 × [Mg + PO_4]) did not differ significantly from control rates at either temperature (all $p \geq 0.97$). These differences resulted in a significant time × treatment × temperature interaction ($F_{7,48} = 49.32$, $p < 0.001$). Elevated temperature significantly increased precipitation rates in the 2 × [Ca], 2 × [Ca + Mg], and 2 × [Ca + PO_4] treatments (all $p < 0.001$) with the strongest effects observed in the 2 × [Ca] treatment, which increased from ~6 NTU·h^{-1} at 12 °C to ~62 NTU·h^{-1} at 18 °C. In contrast, precipitation rates in the 2 × [Ca + Mg + PO_4] treatment did not differ significantly between temperatures ($p = 0.108$). Estimated precipitation rates and full pairwise comparisons are provided in Supplementary Tables S1-S3.

3.2. Final turbidity at 8 h

Final turbidity at 8 h differed significantly among treatments and between temperatures, with a significant treatment × temperature interaction indicating that the effect of temperature varied among treatments ($F_{7,48} = 48.27$, $p < 0.001$) (Fig. 2B). Treatments containing elevated Ca exhibited the greatest turbidity at both temperatures, with turbidity generally increasing from 2 × [Ca] to 2 × [Ca + Mg] and reaching the highest values in PO_4 containing Ca treatments (2 × [Ca + PO_4] and 2 × [Ca + Mg + PO_4]), where maximum turbidity reached ~200 to ~245 NTU. PO_4 containing treatments lacking

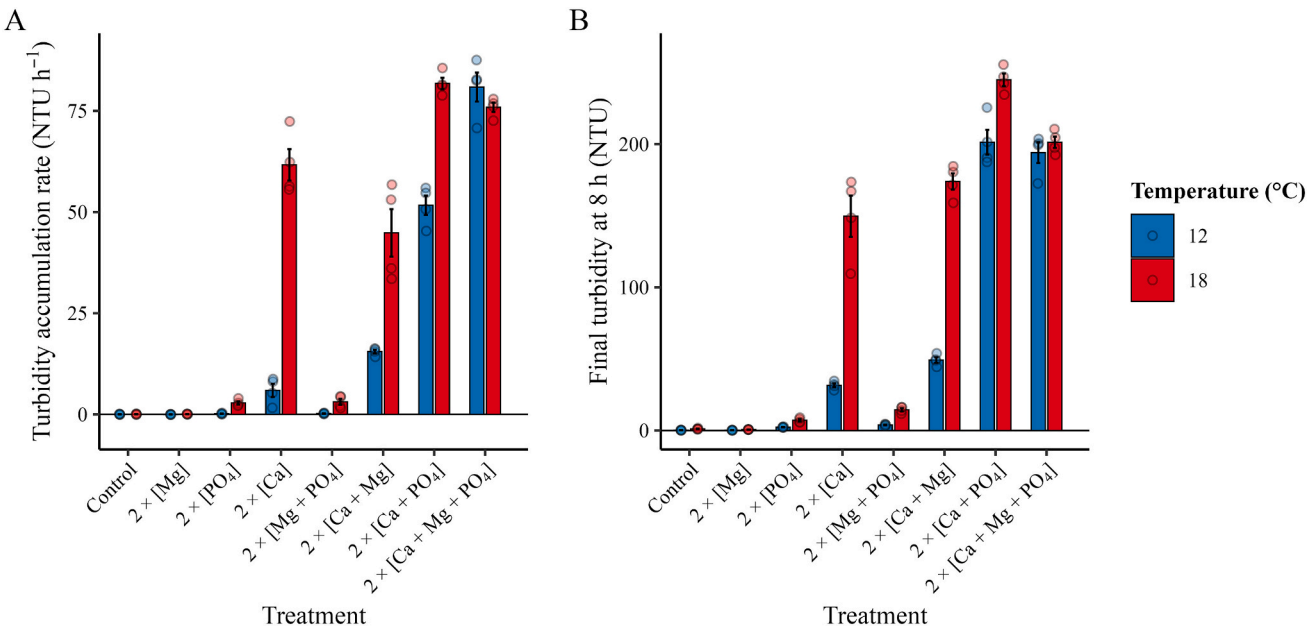


Fig. 2. Precipitation dynamics following CO_2 reduction at 12 °C and 18 °C. (A) Turbidity accumulation rates (NTU·h^{-1}) over 0–2 h. (B) Final turbidity at 8 h. Points represent individual flasks ($N = 4$), with means ± SEM shown. Treatments correspond to increases in ionic composition relative to control. Statistical summaries and pairwise comparisons are provided in Tables S1-S6.

elevated Ca (2 × [PO_4] and 2 × [Mg + PO_4]) exhibited modest but significant increases in turbidity relative to controls at both temperatures. The 2 × [Mg] treatment did not differ significantly from controls at either temperature. Temperature significantly increased turbidity in most treatments, with the strongest increases observed in 2 × [Ca] and 2 × [Ca + Mg] treatments, while no significant temperature effect was detected in the 2 × [Ca + Mg + PO_4] treatment. Mean turbidity (± SEM) at 8 h and full pairwise comparisons are provided in Supplementary Tables S4-S6.

3.3. Turbidity trajectories over time

Turbidity trajectories over the full 0–8 h time course are illustrated qualitatively using Michaelis-Menten fits applied to treatment means across four replicate flasks. Fig. 3A shows the full turbidity range (0–250 NTU), while Fig. 3B scales to the lower turbidity range from (0–50 NTU). These curves illustrate a rapid increase in turbidity during the first 2 h following the reduction from 2% CO_2 to 0.5% CO_2, followed by a progressive slowing of the response over time. Treatments containing elevated Ca exhibited steep initial increases and reached substantially higher maximum turbidity compared to all other treatments. In contrast, treatments without elevated Ca showed more gradual increases and less clear plateauing within the 8 h experimental period.

3.4. Net ion loss following CO_2 trigger

Net changes in dissolved Ca, Mg, and PO_4 following the CO_2 reduction and accompanying pH elevation are shown in Fig. 4. Ca loss differed significantly among treatments ($F_{7,48} = 25.93$, $p < 0.001$). Minimal loss (~ 0 to −0.4 mmol L^{-1}) occurred in control and treatments lacking elevated Ca, whereas all treatments containing elevated Ca exhibited greater depletion. The magnitude of Ca loss generally increased with additional ions, from approximately −0.5 mmol L^{-1} in the 2 × [Ca] treatment to −1.6 mmol L^{-1} in the 2 × [Ca + Mg + PO_4] treatment.

Mg loss differed among treatments ($F_{7,48} = 4.13$, $p = 0.001$), but overall changes were small. The greatest depletion was in the 2 × [Ca + Mg + PO_4] treatment (~ −0.2 mmol L^{-1}), while most other treatments showed minimal net loss (generally ~0 to −0.1 mmol L^{-1}) and were comparable to control values. Residuals deviated from normality; however, the model was retained due to the robustness of ANOVA and consistency of results.

PO_4 loss differed significantly among treatments ($F_{7,48} = 15.83$, $p < 0.001$) and exhibited a significant interaction with temperature ($F_{7,48} = 3.52$, $p = 0.004$). The greatest PO_4 depletion occurred in treatments where Ca and PO_4 were elevated together, particularly the 2 × [Ca + Mg + PO_4] treatment, which reached approximately −1.7 mmol L^{-1} at 12 °C. In contrast, control and most single-ion treatments exhibited comparatively small changes in PO_4 concentration (typically ~0 to −0.7 mmol L^{-1}). Temperature effects varied among treatments, with some treatments exhibiting greater PO_4 depletion at higher temperature. Full model outputs and *post hoc* comparisons for each ion are provided in Tables S7 & S8.

Molar loss ratios of Ca, Mg, and PO_4 (Table 4) showed that treatments exhibiting the greatest ion loss had consistent Ca:PO_4 ratios (~1–1.6:1), whereas treatments with minimal precipitation exhibited highly variable and inconsistent ratios. Across treatments, Mg:PO_4 ratios remained comparatively low, indicating minor Mg incorporation relative to Ca and PO_4.

3.5. X-ray powder diffraction analysis

X-ray diffraction analysis revealed treatment-dependent differences in recovered precipitates (Table S9; Figs. S1-S6). Halite (NaCl) was identified in all samples. In both replicates of the 2 × [Ca + PO_4] treatment, diffraction features were tentatively consistent with poorly crystalline apatite, although phase identification was of low confidence. In contrast, an amorphous phase was identified in both replicates of the 2 × [Ca + Mg + PO_4] treatment. Neither apatite nor an amorphous phase was identified in the 2 × [Ca] treatment. Low-intensity crystalline material that could not be identified was also present in both the 2 × [Ca] and 2 × [Ca + Mg + PO_4].

3.6. Thermodynamic modeling of saturation states

The logarithm of dahllite ($Ca_{10}(PO_4)_6(CO_3)_{0.5}(OH)$) ion activity product exhibited a strong positive relationship with log-transformed

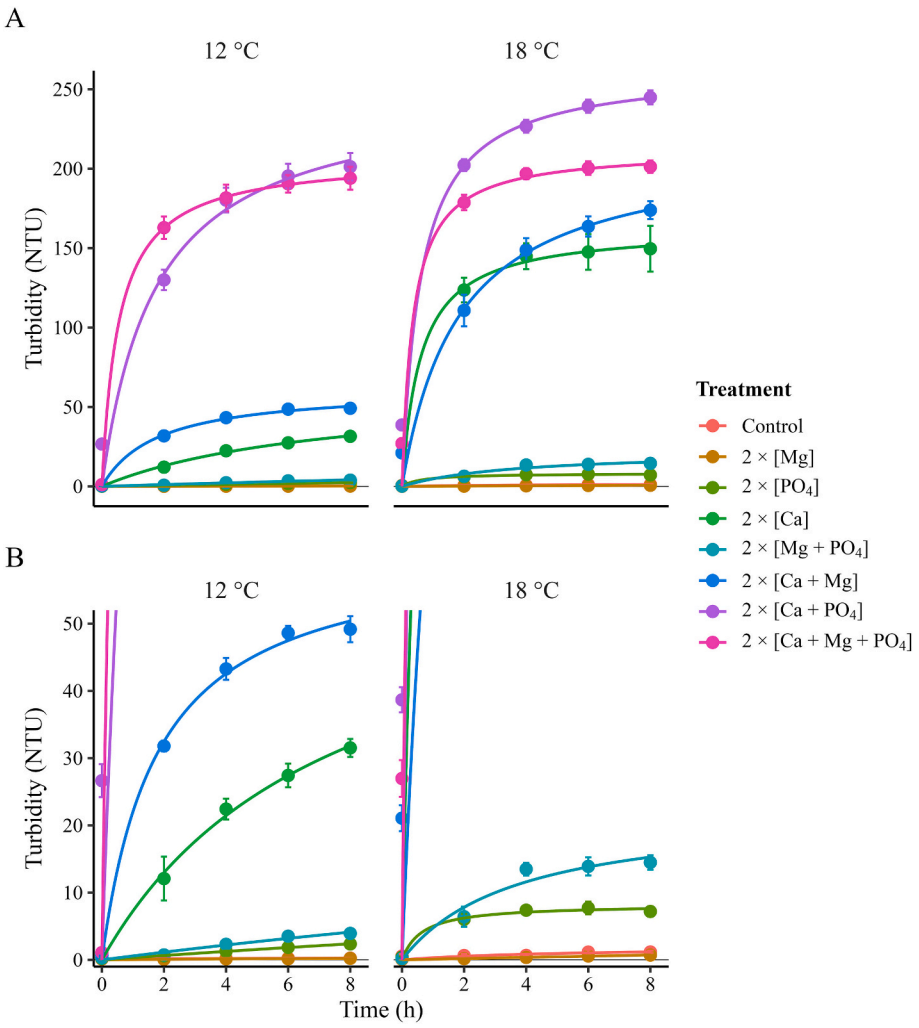


Fig. 3. Turbidity trajectories over the 0–8 h time course at 12 °C and 18 °C. Points represent treatment means ($N = 4$ flasks per treatment), and solid lines show Michaelis-Menten fits applied to mean values. (A) Full turbidity range (0–250 NTU). (B) Expanded view of the lower turbidity range (0–50 NTU).

turbidity at 8 h post-trigger across all ion treatments and temperatures, explaining approximately 95% of the observed variance (Fig. 5). A near-linear relationship was observed across approximately five orders of magnitude in IAP and more than three orders of magnitude in turbidity.

Turbidity generally increased under conditions corresponding to positive SI (SI > 0), consistent with thermodynamically favorable conditions for precipitation. Similar but weaker relationships were observed for other Ca-PO_4 phases, whereas correlations with Mg-PO_4 phases such as newberyite were low.

3.7. Turbidity-precipitate mass relationship

Turbidity increased strongly with precipitate mass across all treatments and temperatures ($R^2 = 0.798$, $p < 0.001$; Fig. 6). This strong positive relationship indicates that turbidity provided a useful proxy for precipitate formation in the experimental system.

4. Discussion

Nephrocalcinosis is increasingly recognized as a multifactorial disorder arising from interactions between environmental and physiological stressors. In the present study, we isolated ionic composition under controlled CO_2 conditions that mimic the hypothesized acid-base dynamics driving nephrocalcinosis, allowing direct evaluation of how individual ions (Ca, Mg and PO_4) influence the initiation and magnitude of precipitation following a CO_2 triggered shift in pH. Although Ca-PO_4 precipitation under supersaturated conditions is well established in the geochemical and biomineralization literature, the present study quantifies how variation in Ca, Mg, and PO_4, which have been implicated in nephrocalcinosis development, modifies the kinetics and the magnitude of precipitation during a standardized CO_2 driven acid-base disturbance relevant to salmonid physiology.

The most prominent finding was that Ca availability governed both the initiation and magnitude of precipitation following the rapid reduction in PCO_2 (the CO_2 trigger). Treatments containing elevated Ca exhibited the highest precipitation rates during the initial 0–2 h period and the greatest final turbidity at 8 h (Fig. 2). In contrast, treatments lacking elevated Ca showed minimal precipitation, even in the presence of elevated Mg and/or PO_4. This pattern indicates that Ca availability was the primary determinant of whether post-trigger chemical conditions resulted in observable precipitation under the tested conditions.

In comparison to our previous work using control pre-urine composition (Emadi et al., 2026), where temperature effects were evident within a narrow turbidity range (~0–3 NTU), the present study exhibited substantially greater precipitation under elevated ionic loading, yet the stimulatory effect of higher temperature remained apparent (Figs. 2, 3). Although temperature effects remain detectable at low turbidity values, their relative influence is reduced compared to the dominant effect of Ca availability under the conditions tested here.

Building on this, PO_4 strongly amplified this response when

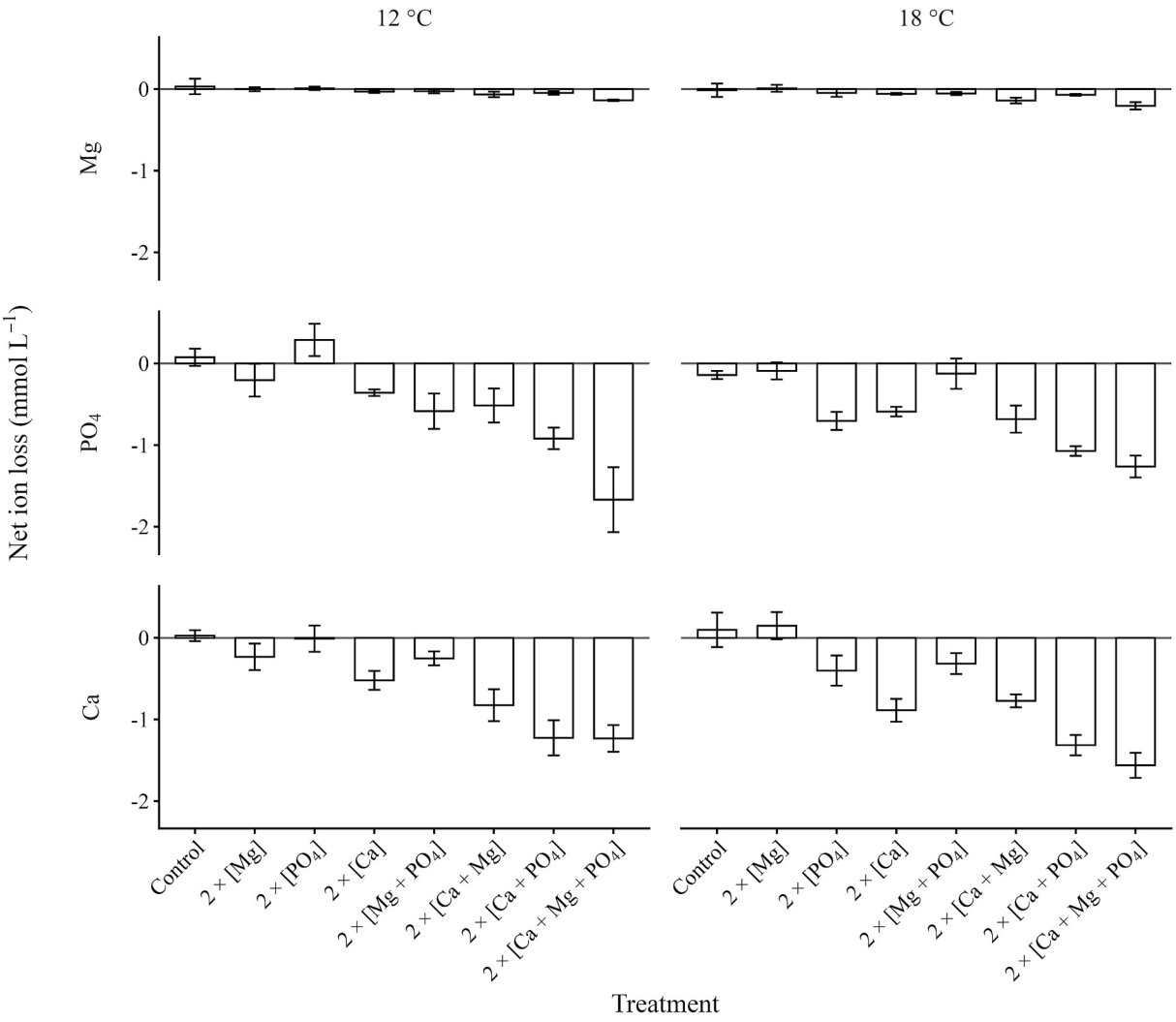


Fig. 4. Net change in dissolved magnesium (Mg), phosphate (PO_4), and calcium (Ca) concentrations (mmol L^{-1}) from the compensated state (0 h) to 8 h at 12 °C and 18 °C. Values represent mean ± SEM ($N = 4$ per treatment). Treatments correspond to increases in ionic composition relative to control. Statistical summaries and pairwise comparisons are provided in Tables S7-S8.

Table 4
Molar loss ratios (Ca:Mg:PO_4) calculated from dissolved ion losses between the compensated state (0 h) and 8 h following the CO_2 trigger. Ratios were normalized to $PO_4 = 1$ to facilitate comparison with expected mineral stoichiometries. Ratios are most meaningful in treatments with substantial ion loss and should be interpreted cautiously where ion changes are minimal.

Treatment	12 °C	18 °C
Control	0.33: −0.30: 1	0.46: 1.04: 1
2 × [Mg]	−11.33: −0.78: 1	0.47: 0.15: 1
2 × [PO_4]	1.16: 0.15: 1	0.53: 0.05: 1
2 × [Ca]	1.43: 0.08: 1	1.64: 0.11: 1
2 × [Mg + PO_4]	0.84: 0.06: 1	−0.40: −0.10: 1
2 × [Ca + Mg]	4.10: 0.72: 1	1.33: 0.24: 1
2 × [Ca + PO_4]	1.45: 0.05: 1	1.23: 0.07: 1
2 × [Ca + Mg + PO_4]	0.80: 0.09: 1	1.30: 0.17: 1

combined with Ca (Figs. 2, 3). Elevated PO_4 alone produced relatively minor precipitation, and Ca alone generated a more moderate response; however, their combination produced substantially greater turbidity than either ion independently. This interaction is consistent with the dominance of Ca-PO_4 phases such as carbonate apatite ($Ca_{10}(PO_4)_6CO_3$) and brushite ($CaHPO_4{\cdot}H_2O$) in nephrocalcinosis deposits (Klykken et al., 2022), and highlights PO_4 as a key amplifier of Ca-driven precipitation once sufficient supersaturation is achieved (Song et al., 2002).

Mg exerted a secondary and context-dependent influence on precipitation. Mg alone had little effect, and its influence in Ca-containing treatments was not consistent across conditions. In treatments containing both elevated Ca and PO_4, the addition of Mg did not substantially increase final precipitation relative to Ca and PO_4 alone. Although final turbidity tended to be slightly lower at 18 °C when Mg was added to the elevated Ca and PO_4 treatment, this effect was not statistically significant. These results indicate that Mg is not a primary driver of precipitation in this system, and that its effects, where present, were secondary to the stronger influence of Ca-PO_4 interactions.

Temperature effects on precipitation varied among treatments and between time scales. Increasing temperature enhanced precipitation in Ca-containing solutions, but this was not observed in the 2 × [Ca + Mg + PO_4] treatment, where responses were similar between 12 °C and 18 °C despite rapid initial precipitation (Figs. 2, 3). This pattern suggests that precipitation in this treatment approached a limiting state within the initial 0–2 h timeframe, reducing the ability to detect temperature-dependent differences. As such, the lack of a temperature effect in this treatment may reflect limitations on observable precipitation dynamics rather than a direct suppression of temperature sensitivity.

These patterns indicate that the strong influence of Ca and PO_4 on

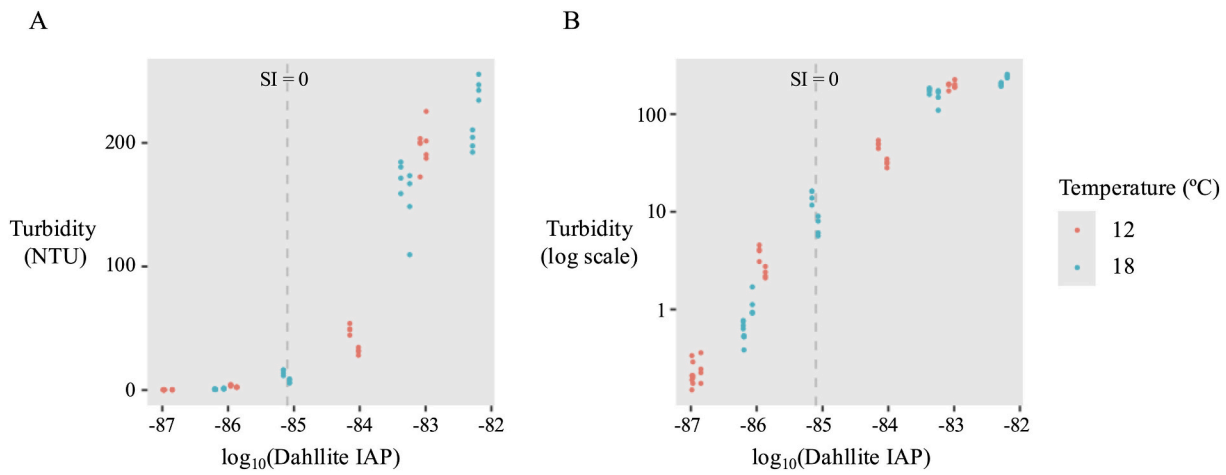


Fig. 5. Relationship between modeled dahllite ion activity product (IAP) and observed turbidity at 8 h post-trigger across ion treatment and temperatures. Panel A shows raw turbidity values, while Panel B shows log-transformed turbidity. Dashed vertical lines indicate the approximate theoretical saturation threshold corresponding to a saturation index (SI) = 0 for dahllite based on thermodynamic parameters derived from the JESS database (Bonet et al., 2023).

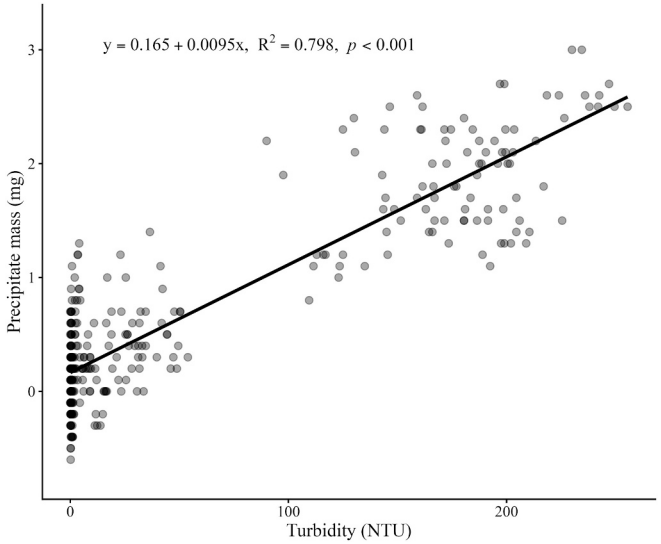


Fig. 6. Relationship between turbidity (NTU) and precipitate mass (mg) across treatments and temperatures. Precipitate mass was determined from a fixed sample volume (10 mL) for all treatments. Points represent individual observations; darker points indicate overlapping observations caused by point transparency. The solid line indicates the fitted linear regression.

precipitation reflects their contribution to solution supersaturation, whereas the resulting mineral phase and precipitation dynamics are governed by kinetic processes, including nucleation and crystal growth (Cao and Harris, 2008; Mejri et al., 2013; Pan et al., 2013). Klykken et al. (2022) observed that "amorphous carbonate apatite" was the dominant mineral phase in salmon nephrocalcinosis, suggesting that amorphous or poorly crystalline phases may be important during nephrocalcinosis development. Such phases can form rapidly under supersaturated conditions and can subsequently transform into more stable crystalline forms depending on solution chemistry and time (Blue et al., 2017; Blue and Dove, 2015).

This framework aligns with the present results, where net ion analysis demonstrated that precipitation was dominated by removal of Ca and PO_4 from solution (Fig. 4), while Mg exhibited comparatively little depletion, suggesting that Mg was not a major component of the precipitate. Molar loss ratios (Table 4) further support this pattern, with Ca:PO_4 ratios in treatments exhibiting the greatest precipitation ranging from ~1–1.6:1, consistent with Ca-PO_4 stoichiometries, while Mg:PO_4 loss ratios were low (~0.1:1), consistent with comparatively little incorporation of Mg into the precipitate. These patterns are not compatible with Mg-dominated mineral phases such as struvite ($MgNH_4PO_4{\cdot}6H_2O$) and newberyite ($MgHPO_4{\cdot}3H_2O$). Furthermore, previous work has shown that newberyite is stable primarily under acidic conditions and becomes unstable above ~ pH 6.5, making its formation unlikely under the alkaline conditions in the present study. Treatments containing elevated Ca and PO_4 produced the greatest ion loss, further supporting the prevalence of Ca-PO_4 precipitation. Qualitatively, the precipitate appeared as a fine white particulate that gradually settled out of suspension when mixing ceased, resembling descriptions of early stage nephrocalcinosis deposits in salmonids.

The XRD results provide additional support for Ca-PO_4 mineral formation while also suggesting that ionic composition may influence the nature of the resulting precipitate. The tentative identification of poorly crystalline apatite in the 2 × [Ca + PO_4] treatment is consistent with the observed removal of Ca and PO_4 from solution and with the prevalence of Ca-PO_4 phases reported in nephrocalcinosis deposits (Klykken et al., 2022). Notably, when Mg was also elevated in the 2 × [Ca + Mg + PO_4] treatment, an amorphous phase was detected rather than the poorly crystalline apatite signature in the 2 × [Ca + PO_4] treatment. Previous studies have shown that Mg can inhibit Ca-PO_4 crystallization and promote the formation of amorphous calcium phosphate, providing a potential explanation for the difference observed between these treatments (Cao and Harris, 2008). However, the composition of the amorphous material could not be determined by XRD, and the addition of Mg did not significantly alter the overall magnitude of precipitation. Halite (NaCl) was also identified in all samples; however, given the high NaCl concentrations of the synthetic pre-urine and subsequent drying of the recovered precipitates, this likely reflects crystallization of residual NaCl during sample preparation rather than mineral precipitation associated with the experimental trigger.

The thermodynamic modeling further supports this interpretation. Importantly, the modeled dahllite ion activity products were calculated entirely independently from the precipitation data, using published thermodynamic parameters and simulated initial solutions matching the formulations described in Methods. Despite this independence, modeled dahllite ion activity products showed a strong positive relationship with observed turbidity across treatments and temperatures (Fig. 5). This relationship suggests that thermodynamic modeling captures an important component of the precipitation dynamics relevant to nephrocalcinosis and can quickly generate predictions and hypotheses about precipitation risk across a wide range of ion compositions and CO_2-

trigger scenarios. The interplay between *in vitro* and *in silico* modeling thus holds great promise for accelerating research on mineralopathies.

Although these results do not demonstrate that dahllite itself was the precipitated mineral phase, dahllite represented the closest available thermodynamic proxy for carbonate containing Ca-PO_4 phases. The comparatively weaker relationships observed for Mg-PO_4 phases further support the interpretation that precipitation in the present system was dominated primarily by Ca-PO_4 chemistry. However, the present experiments examined only a limited region of the ion-composition space, and under alternative ionic conditions, such as those with greater Mg enrichment and/or addition of ammonium (NH_4^+), other mineral phases may become thermodynamically relevant predictors of precipitation behaviour. Such scenarios could be further investigated using *in silico* thermodynamic modeling where different mineral phases are allowed to compete.

Together, these results support a model in which rapid pH elevation following the CO_2 trigger promotes Ca-PO_4 precipitation under conditions of elevated supersaturation, which likely governs early precipitation dynamics. This framework is consistent with the proposed mechanism in fish, where HCO_3^- accumulation during compensation followed by rapid CO_2 reduction leads to transient alkalosis, creating conditions that are favorable for mineral precipitation (Takvam et al., 2021).

A more mechanistic interpretation of the experimental trigger is that it does not directly initiate precipitation but instead induces supersaturation by shifting carbonate equilibria and increasing pH. The magnitude of this response is strongly influenced by prior CO_2 exposure history. Under conditions of chronic hypercapnia, fish compensate for respiratory acidosis through elevation of plasma HCO_3^- in exchange for chloride (Brauner et al., 2019; Tovey and Brauner, 2018). If CO_2 is rapidly reduced, this elevated HCO_3^- pool cannot be immediately excreted, resulting in a transient but pronounced alkalosis that can lead to a greater increase in pH and, as a result, a higher degree of supersaturation (Perry et al., 2010). Consistent with this, greater increases in pH (ΔpH) were associated with increased precipitation in our previous work (Emadi et al., 2026).

Additionally, increased ionic loading from feed or water may elevate plasma concentrations of Ca, Mg, and PO_4, increasing their filtration into the pre-urine and thereby increasing the thermodynamic potential for precipitation (Bucking et al., 2010; Sugiura, 2025; Sugiura et al., 2000; Takvam et al., 2021; Wheatly et al., 1984; Wood, 1995). Together, differences in overall ionic load (feed and/or water) may help explain the limited effects of elevated CO_2 exposure on nephrocalcinosis development in some studies (Good et al., 2018; Good et al., 2010; Mota et al., 2019), compared to others (Fivelstad et al., 2018; Fivelstad et al., 2003; Hosfeld et al., 2008). In systems where CO_2 is maintained at moderate levels, the alkalosis-driven increase in supersaturation associated with rapid CO_2 reduction may be absent, however, under conditions of sufficiently high ionic loading, precipitation may still occur in the absence of a strong CO_2-driven trigger, as suggested by observations linking salinity-driven ion loading (salinity: 3–5 ppt) to nephrocalcinosis risk (Klykken et al., 2023) and by studies reporting limited or inconsistent relationships between moderate CO_2 levels and nephrocalcinosis prevalence (Sissener et al., 2026).

Building on this framework, the extent of precipitation depends not only on the degree of supersaturation but also on the duration of exposure to these conditions. In seawater or high salinity environments, reduced flow and increased retention time of the filtrate in the renal system may prolong supersaturated conditions and increase the likelihood of precipitation (Damsgaard et al., 2020; Takvam et al., 2023; Takvam et al., 2021). Within the renal system, crystal formation proceeds through nucleation, growth, and aggregation, and increased residence time allows particles more time to grow and coalesce, increasing the probability of retention (Kok and Khan, 1994). Extended residence time may allow initial precipitates to undergo further growth and transformation toward more stable crystalline phases, increasing the likelihood of persistent mineral deposition (Whittaker et al., 2016). This framework is consistent with production-scale observations indicating that nephrocalcinosis severity often increases following salinity protocols (5–12 ppt) (Klykken et al., 2023; Klykken et al., 2022), when glomerular filtration rate and urine flow rate are known to be greatly reduced (Damsgaard et al., 2020; Wood, 1995), which would increase urine residence time. In addition, increased NaCl-coupled water reabsorption through the renal system may further concentrate Ca, Mg and PO_4 in the urine, promoting supersaturation (Marshall, 1995; McDonald and Grosell, 2006; Renfro, 1975). Therefore, early-stage mineral formation may be exacerbated under conditions that promote prolonged supersaturation through altered urine chemistry and reduced urine flow, conditions that may become more prevalent under intensive aquaculture scenarios involving salinity management and other husbandry practices that can alter urinary chemistry and increase ionic loading (Sommerset et al., 2024).

A limitation of the present study is that it was conducted over an 8 h period and therefore does not capture longer-term precipitation dynamics or the continual contribution of ions from the filtrate that would occur *in vivo*. Additionally, HCO_3^- would be expected to slowly decrease *in vivo* over this period while fish are adjusting to lower PCO_2 in the water (Perry et al., 2010; Wheatly et al., 1984), whereas in our model system HCO_3^- concentration in the simulated pre-urine is kept high after the trigger (Emadi et al., 2026). Synthetic pre-urine also lacks proteins and other organic components that may influence nucleation processes and therefore may not fully represent later stages of nephrocalcinosis, where renal damage, including glomerular impairment, could alter the urinary composition through protein leakage (proteinuria) or release of organic materials (Haraldsson et al., 2008). Additionally, the thermodynamic modeling performed did not incorporate explicit precipitation kinetics. Ca-PO_4 systems can exhibit metastability, nucleation barriers, and kinetic inhibition, meaning that supersaturation conditions do not necessarily result in immediate crystal growth or mineral retention *in vivo* (Wang and Nancollas, 2008). XRD characterization was limited to representative 8 h treatments which yielded sufficient recovered precipitate for analysis, preventing mineralogical characterization of treatments from earlier time points. Furthermore, XRD could not determine the composition of the amorphous material identified in the 2 × [Ca + Mg + PO_4] treatment. Lastly, while turbidity provided a useful real-time indicator of the presence and dynamics of precipitation (Fan and Castleberry, 2023), it does not directly measure the extent of precipitation, as turbidity is influenced by particle size, shape, and aggregation state. Accordingly, turbidity was interpreted alongside precipitate mass (Fig. 6), which showed a strong overall relationship with turbidity, and ion removal to provide complementary measures of precipitation (Morrison et al., 2014).

5. Conclusion

Analyses of risk factors and experimental observations have consistently identified elevated CO_2 and ionic loading as a central component of nephrocalcinosis etiology. However, the complexity of interacting environmental and physiological factors in aquaculture systems has limited the ability to resolve how acid-base dynamics and ionic composition interact to drive precipitation, as well as the relative contributions of Ca, Mg and PO_4.

By isolating these factors under controlled CO_2-driven acid-base conditions, the present study provides insights into these interactions. Within this framework, Ca emerged as the primary driver of mineral precipitation, PO_4 acted as a key amplifier of Ca driven responses, and Mg exerted a minimal and secondary role on precipitation dynamics. XRD analysis of representative precipitates further indicated the formation of poorly crystalline or amorphous material, with a tentative poorly crystalline apatite signature observed under elevated Ca and PO_4 and an amorphous phase detected when Mg was also elevated. Supporting these findings, thermodynamic modeling demonstrated that

modeled ion activity products strongly predicted precipitation responses across ion treatments and temperature, highlighting supersaturation as a key driver of mineral formation under the tested conditions.

Together, these results support a model in which nephrocalcinosis risk may arise from the interaction between (1) the magnitude of CO_2 driven acid-base disturbance, specifically the transition from compensated respiratory acidosis to post-trigger alkalosis, (2) the degree of ionic loading, and (3) the duration of supersaturation within the renal system. This provides a mechanistic basis for interpreting production-scale observations linking CO_2 fluctuations, water chemistry, and seawater transfer to disease onset in salmonid aquaculture.

Author contribution

CMW, MT, TON, and CJB developed the *in vivo* model. JOV developed the *in silico* model. CE developed the *in vitro* methodology and performed all experiments. CMW, CJB, and TON provided supervision. TON secured funding. CE wrote the first draft of the MS, and all authors edited it.

Declaration of generative AI and AI-assisted technologies in the manuscript preparation process

During the preparation of this work, the authors used ChatGPT Pro to assist with the development and troubleshooting of the thermodynamic modeling workflow and computational implementation of the *in-silico* analyses. After using this tool/service, the authors reviewed and edited the content as needed and take full responsibility for the content of the published article.

CRediT authorship contribution statement

Cameron M. Emadi: Writing – review & editing, Writing – original draft, Visualization, Validation, Project administration, Methodology, Investigation, Formal analysis, Data curation, Conceptualization. **Jon Olav Vik:** Writing – review & editing, Visualization, Validation, Software, Resources, Methodology, Formal analysis. **Marius Takvam:** Writing – review & editing, Methodology, Conceptualization. **Tom Ole Nilsen:** Writing – review & editing, Project administration, Methodology, Funding acquisition, Conceptualization. **Colin J. Brauner:** Writing – review & editing, Validation, Supervision, Resources, Project administration, Methodology, Funding acquisition, Conceptualization. **Chris M. Wood:** Writing – review & editing, Validation, Supervision, Resources, Project administration, Methodology, Funding acquisition, Conceptualization.

Declaration of competing interest

The authors declare that they have no known competing financial interests or personal relationships that could have appeared to influence the work reported in this paper.

Acknowledgments

The work was funded by the Norwegian Seafood Research Fund under grant agreement FHF-901874. We thank Dr. Cole Mauws of the UBC Electron Microbeam/X-Ray Diffraction Facility for assistance with X-ray powder diffraction analysis and phase identification.

Appendix A. Supplementary data

Supplementary data to this article can be found online at https://doi.org/10.1016/j.aquaculture.2026.744627.

Data availability

Data will be made available on request.

References

Bates, D., Mächler, M., Bolker, B., Walker, S., 2015. Fitting linear mixed-effects models using lme4. J. Stat. Softw. 67, 1–48. https://doi.org/10.18637/jss.v067.i01.

Blue, C.R., Dove, P.M., 2015. Chemical controls on the magnesium content of amorphous calcium carbonate. Geochim. Cosmochim. Acta 148, 23–33. https://doi.org/10.1016/j.gca.2014.08.003.

Blue, C.R., Giuffre, A., Mergelsberg, S., Han, N., Yoreo, J.J.D., Dove, P.M., 2017. Chemical and physical controls on the transformation of amorphous calcium carbonate into crystalline $CaCO_3$ polymorphs. Geochim. Cosmochim. Acta 196, 179–196. https://doi.org/10.1016/j.gca.2016.09.004.

Bonet, J., Filella, M., May, P.M., May, R.F., Murray, K., 2023. JESS Thermodynamic database of chemical reactions. https://doi.org/10.5281/zenodo.7700024.

Boutilier, R.G., Heming, T.A., Iwama, G.K., 1984. Appendix: physicochemical parameters for use in fish respiratory physiology. Fish Physiol. 10, 403–430. https://doi.org/10.1016/s1546-5098(08)60323-4.

Brauner, C.J., Shartau, R.B., Damsgaard, C., Esbaugh, A.J., Wilson, R.W., Grosell, M., 2019. Acid-base physiology and CO_2 homeostasis: regulation and compensation in response to elevated environmental CO_2. In: Fish Physiol., pp. 69–132. https://doi.org/10.1016/bs.fp.2019.08.003.

Brauner, C.J., Thorarensen, H., Gallaugher, P., Farrell, A.P., Randall, D.J., 2000. CO_2 transport and excretion in rainbow trout (*Oncorhynchus mykiss*) during graded sustained exercise. Respir. Physiol. 119, 69–82. https://doi.org/10.1016/s0034-5687(99)00091-2.

Bucking, C., Landman, M.J., Wood, C.M., 2010. The role of the kidney in compensating the alkaline tide, electrolyte load, and fluid balance disturbance associated with feeding in the freshwater rainbow trout, *Oncorhynchus mykiss*. Comp. Biochem. Physiol. A Mol. Integr. Physiol. 156, 74–83. https://doi.org/10.1016/j.cbpa.2009.12.021.

Cao, X., Harris, W., 2008. Carbonate and magnesium interactive effect on calcium phosphate precipitation. Environ. Sci. Technol. 42, 436–442. https://doi.org/10.1021/es0716709.

Charlton, S.R., Parkhurst, D.L., Appelo, C.A.J., Cohen, S.D., Hindmarsh, A.C., Serban, R., Shumaker, D., CVODE/SUNDIALS, A.G.T. for, 2014. Phreeqc: R Interface to Geochemical Modeling Software. CRAN: Contrib. Packag. https://doi.org/10.32614/cran.package.phreeqc

Dalum, A.S., Alarcon, M., Gretarsson, P., Reed, A.K., Wisløff, H., McDougall, K.K., Takvam, M., 2025. Characterisation of urocystolithiasis in farmed Atlantic salmon (*Salmo salar* L.): histopathological features and pathophysiological considerations. J. Fish Dis., e70099 https://doi.org/10.1111/jfd.70099.

Damsgaard, C., McGrath, M., Wood, C.M., Richards, J.G., Brauner, C.J., 2020. Ion-regulation, acid/base-balance, kidney function, and effects of hypoxia in coho salmon, *Oncorhynchus kisutch*, after long-term acclimation to different salinities. Aquaculture 528, 735571. https://doi.org/10.1016/j.aquaculture.2020.735571.

Elzhov, T.V., Mullen, K.M., Spiess, A.-N., Bolker, B., 2023. Minpack.lm: R Interface to the Levenberg-Marquardt Nonlinear Least-squares Algorithm Found in MINPACK, Plus Support for Bounds.

Emadi, C.M., Wood, C.M., Takvam, M., Nilsen, T.O., Brauner, C.J., 2026. Simulating nephrocalcinosis in a jar: an in vitro temperature-dependent model of CO_2-induced precipitation relevant to intensive aquaculture. Aquaculture 613, 743354. https://doi.org/10.1016/j.aquaculture.2025.743354.

Fan, Y., Castleberry, S., 2023. High-throughput kinetic turbidity analysis for determination of amorphous solubility and excipient screening for amorphous solid dispersions. Int. J. Pharm. 631, 122495. https://doi.org/10.1016/j.ijpharm.2022.122495.

Fivelstad, S., Hosfeld, C.D., Medhus, R.A., Olsen, A.B., Kvamme, K., 2018. Growth and nephrocalcinosis for Atlantic salmon (*Salmo salar* L.) post-smolt exposed to elevated carbon dioxide partial pressures. Aquaculture 482, 83–89. https://doi.org/10.1016/j.aquaculture.2017.09.012.

Fivelstad, S., Olsen, A.B., Åsgård, T., Baeverfjord, G., Rasmussen, T., Vindheim, T., Stefansson, S., 2003. Long-term sublethal effects of carbon dioxide on Atlantic salmon smolts (*Salmo salar* L.): ion regulation, haematology, element composition, nephrocalcinosis and growth parameters. Aquaculture 215, 301–319. https://doi.org/10.1016/s0044-8486(02)00048-0.

Good, C., Davidson, J., Terjesen, B.F., Takle, H., Kolarevic, J., Bæverfjord, G., Summerfelt, S., 2018. The effects of long-term 20 mg/L carbon dioxide exposure on the health and performance of Atlantic salmon *Salmo salar* post-smolts in water recirculation aquaculture systems. Aquac. Eng. 81, 1–9. https://doi.org/10.1016/j.aquaeng.2018.01.003.

Good, C., Davidson, J., Welsh, C., Snekvik, K., Summerfelt, S., 2010. The effects of carbon dioxide on performance and histopathology of rainbow trout *Oncorhynchus mykiss* in water recirculation aquaculture systems. Aquac. Eng. 42, 51–56. https://doi.org/10.1016/j.aquaeng.2009.11.001.

Haraldsson, B., Nyström, J., Deen, W.M., 2008. Properties of the glomerular barrier and mechanisms of proteinuria. Physiol. Rev. 88, 451–487. https://doi.org/10.1152/physrev.00055.2006.

Hosfeld, C.D., Engevik, A., Mollan, T., Lunde, T.M., Waagbø, R., Olsen, A.B., Breck, O., Stefansson, S., Fivelstad, S., 2008. Long-term separate and combined effects of environmental hypercapnia and hyperoxia in Atlantic salmon (*Salmo salar* L.) smolts. Aquaculture 280, 146–153. https://doi.org/10.1016/j.aquaculture.2008.05.009.

Klykken, C., Khan, E., Karlsen, C., Reed, A.K., Attramadal, K.J.K., Olsen, R.E., Boissonnot, L., 2023. Nephrocalcinosis in juvenile farmed Atlantic salmon (*Salmo salar*) may be linked to osmoregulatory stress. J. Fish Dis. 46, 943–956. https://doi.org/10.1111/jfd.13815.

Klykken, C., Reed, A.K., Dalum, A.S., Olsen, R.E., Moe, M.K., Attramadal, K.J.K., Boissonnot, L., 2022. Physiological changes observed in farmed Atlantic salmon (*Salmo salar* L.) with nephrocalcinosis. Aquaculture 554, 738104. https://doi.org/10.1016/j.aquaculture.2022.738104.

Kok, D.J., Khan, S.R., 1994. Calcium oxalate nephrolithiasis, a free or fixed particle disease. Kidney Int. 46, 847–854. https://doi.org/10.1038/ki.1994.341.

Landolt, M.L., 1975. Visceral granuloma and nephrocalcinosis of trout. In: Ribelin, W.E., Migaki, G. (Eds.), The Pathology of Fishes. University of Wisconsin Press, Madison, Wisconsin, pp. 793–801.

Lenth, R.V., 2025. Emmeans: Estimated Marginal Means, Aka Least-squares Means.

Marshall, W.S., 1995. 1. Transport processes in isolated teleost epithelia: opercular epithelium and urinary bladder. Fish Physiol. 14, 1–23. https://doi.org/10.1016/s1546-5098(08)60240-x.

McDonald, M.D., Grosell, M., 2006. Maintaining osmotic balance with an aglomerular kidney. Comp. Biochem. Physiol. A Mol. Integr. Physiol. 143, 447–458. https://doi.org/10.1016/j.cbpa.2005.12.029.

Mejri, W., Korchef, A., Tlili, M., Amor, M.B., 2013. Effects of temperature on precipitation kinetics and microstructure of calcium carbonate in the presence of magnesium and sulphate ions. Desalin. Water Treat. 52, 4863–4870. https://doi.org/10.1080/19443994.2013.808813.

Minarova, H., Palikova, M., Kopp, R., Maly, O., Mares, J., Mikulikova, I., Papezikova, I., Piacek, V., Pojezdal, L., Pikula, J., 2023. Nephrocalcinosis in farmed salmonids: diagnostic challenges associated with low performance and sporadic mortality. Front. Vet. Sci. 10, 1121296. https://doi.org/10.3389/fvets.2023.1121296.

Moldal, T., Wiik-Nielsen, J., de Oliveira, V.H.S., Svendsen, J.C., Haukaas, A., Sommerset, I., 2025. Norwegian Fish Health Report 2024. Norwegian Veterinary Institute.

Morrison, J.S., Nophsker, M.J., Haskell, R.J., 2014. A combination turbidity and supernatant microplate assay to rank-order the supersaturation limits of early drug candidates. J. Pharm. Sci. 103, 3022–3032. https://doi.org/10.1002/jps.24090.

Mota, V.C., Nilsen, T.O., Gerwins, J., Gallo, M., Kolarevic, J., Krasnov, A., Terjesen, B.F., 2020. Molecular and physiological responses to long-term carbon dioxide exposure in Atlantic salmon (*Salmo salar*). Aquaculture 519, 734715. https://doi.org/10.1016/j.aquaculture.2019.734715.

Mota, V.C., Nilsen, T.O., Gerwins, J., Gallo, M., Ytteborg, E., Baeverfjord, G., Kolarevic, J., Summerfelt, S.T., Terjesen, B.F., 2019. The effects of carbon dioxide on growth performance, welfare, and health of Atlantic salmon post-smolt (*Salmo salar*) in recirculating aquaculture systems. Aquaculture 498, 578–586. https://doi.org/10.1016/j.aquaculture.2018.08.075.

Murphy, J., Riley, J.P., 1962. A modified single solution method for the determination of phosphate in natural waters. Anal. Chim. Acta 27, 31–36.

Pan, H., Jiang, S., Zhang, T., Tang, R., 2013. In situ solution study of calcium phosphate crystallization kinetics. Methods Enzymol. 129–144. https://doi.org/10.1016/b978-0-12-416617-2.00006-0.

Parkhurst, D.L., Appelo, C.A.J., 2013. Description of Input and Examples for PHREEQC Version 3: A Computer Program for Speciation, Batch-Reaction, One-Dimensional Transport, and Inverse Geochemical Calculations. Tech. Methods. https://doi.org/10.3133/tm6a43.

Perry, S.F., Braun, M.H., Genz, J., Vulesevic, B., Taylor, J., Grosell, M., Gilmour, K.M., 2010. Acid–base regulation in the plainfin midshipman (*Porichthys notatus*): an aglomerular marine teleost. J. Comp. Physiol. B. 180, 1213–1225. https://doi.org/10.1007/s00360-010-0492-8.

Pfalzgraff, T., Volkoff, H., Iburg, T.M., Amlund, H., Skov, P.V., 2025. Growth, appetite, and mineral deposition in rainbow trout reared in fresh- or seawater under different CO_2 regimes. Aquaculture 600, 742234. https://doi.org/10.1016/j.aquaculture.2025.742234.

Program, M.L.T.E.R, 2011. Limnological Methods Manual. McMurdo Long Term Ecological Research Program, McMurdo Station, Antarctica.

Ratkalkar, V.N., Kleinman, J.G., 2011. Mechanisms of stone formation. Clin. Rev. Bone Miner. Metab. 9, 187–197. https://doi.org/10.1007/s12018-011-9104-8.

Renfro, J., 1975. Water and ion transport by the urinary bladder of the teleost *Pseudopleuronectes americanus*. Am. J. Physiol. Legacy Content 228, 52–61. https://doi.org/10.1152/ajplegacy.1975.228.1.52.

Sissener, N.H., Rasmussen, J., Hevroy, E., Philip, A.J.P., 2026. Nephrocalsinosis and mineral deposition in Atlantic salmon (*Salmo salar* L.) during smoltification under different commercial rearing conditions. Aquacult. Rep. 48, 103572. https://doi.org/10.1016/j.aqrep.2026.103572.

Smart, G.R., Knox, D., Harrison, J.G., Ralph, J.A., Richard, R.H., Cowey, C.B., 1979. Nephrocalcinosis in rainbow trout *Salmo gairdneri* Richardson; the effect of exposure to elevated CO_2 concentrations. J. Fish Dis. 2, 279–289. https://doi.org/10.1111/j.1365-2761.1979.tb00170.x.

Sommerset, I., Wiik-Nielsen, J., Oliveira, V.H., Moldal, T., Bornø, G., Haukaas, A., Brun, E., 2024. Norwegian Fish Health Report 2023. Norwegian Veterinary Institute.

Song, Y., Hahn, H.H., Hoffmann, E., 2002. Effects of solution conditions on the precipitation of phosphate for recovery a thermodynamic evaluation. Chemosphere 48, 1029–1034. https://doi.org/10.1016/s0045-6535(02)00183-2.

Sugiura, S.H., 2025. Urinary phosphorus excretion in fish: environmental and aquaculture implications. Aquat. Living Resour. 38, 7. https://doi.org/10.1051/alr/2025004.

Sugiura, S.H., Dong, F.M., Hardy, R.W., 2000. A new approach to estimating the minimum dietary requirement of phosphorus for large rainbow trout based on nonfecal excretions of phosphorus and nitrogen. J. Nutr. 130, 865–872. https://doi.org/10.1093/jn/130.4.865.

Takvam, M., Wood, C.M., Kryvi, H., Nilsen, T.O., 2021. Ion transporters and osmoregulation in the kidney of teleost fishes as a function of salinity. Front. Physiol. 12, 664588. https://doi.org/10.3389/fphys.2021.664588.

Takvam, M., Wood, C.M., Kryvi, H., Nilsen, T.O., 2023. Role of the kidneys in acid-base regulation and ammonia excretion in freshwater and seawater fish: implications for nephrocalcinosis. Front. Physiol. 14, 1226068. https://doi.org/10.3389/fphys.2023.1226068.

Tovey, K.J., Brauner, C.J., 2018. Effects of water ionic composition on acid–base regulation in rainbow trout, during hypercarbia at rest and during sustained exercise. J. Comp. Physiol. B. 188, 295–304. https://doi.org/10.1007/s00360-017-1129-y.

Wang, L., Nancollas, G.H., 2008. Calcium orthophosphates: crystallization and dissolution. Chem. Rev. 108, 4628–4669. https://doi.org/10.1021/cr0782574.

Wheatly, M.G., Hōbe, H., Wood, C.M., 1984. The mechanisms of acid-base and ionoregulation in the freshwater rainbow trout during environmental hyperoxia and subsequent normoxia. II. The role of the kidney. Respir. Physiol. 55, 155–173. https://doi.org/10.1016/0034-5687(84)90020-3.

Whittaker, M.L., Dove, P.M., Joester, D., 2016. Nucleation on surfaces and in confinement. MRS Bull. 41, 388–392. https://doi.org/10.1557/mrs.2016.90.

Wolf, K., 1963. Physiological salines for fresh-water teleosts. Prog. Fish Cult. 25, 135–140. https://doi.org/10.1577/1548-8659(1963)25[135:psfft]2.0.co;2.

Wood, C.M., 1995. Excretion. In: Groot, C., Margolis, L., Clarke, W.C. (Eds.), Physiological Ecology of the Pacific Salmon. UBC Press, Vancouver, BC, pp. 381–438.